Microtubule-dependent pushing forces contribute to long-distance aster movement and centration in *Xenopus laevis* egg extracts

Taylor Sulerud[a,b], Abdullah Bashar Sami[a], Guihe Li[c], April Kloxin[d], John Oakey[b,c], and Jesse Gatlin[a,b,*]

[a]Department of Molecular Biology and [c]Department of Chemical Engineering, University of Wyoming, Laramie, WY 82071; [b]Cell Organization and Division Group, Marine Biological Laboratory, Woods Hole, MA 02543; [d]Department of Chemical and Biomolecular Engineering, University of Delaware, Newark, DE 19716

ABSTRACT **During interphase of the eukaryotic cell cycle, the microtubule (MT) cytoskeleton serves as both a supportive scaffold for organelles and an arborized system of tracks for intracellular transport. At the onset of mitosis, the position of the astral MT network, specifically its center, determines the eventual location of the spindle apparatus and ultimately the cytokinetic furrow. Positioning of the MT aster often results in its movement to the center of a cell, even in large blastomeres hundreds of microns in diameter. This translocation requires positioning forces, yet how these forces are generated and then integrated within cells of various sizes and geometries remains an open question. Here we describe a method that combines microfluidics, hydrogels, and *Xenopus laevis* egg extract to investigate the mechanics of aster movement and centration. We determined that asters were able to find the center of artificial channels and annular cylinders, even when cytoplasmic dynein-dependent pulling mechanisms were inhibited. Characterization of aster movement away from V-shaped hydrogel barriers provided additional evidence for a MT-based pushing mechanism. Importantly, the distance over which this mechanism seemed to operate was longer than that predicted by radial aster growth models, agreeing with recent models of a more complex MT network architecture within the aster.**

Monitoring Editor
Claire Walczak
Indiana University

Received: Feb 3, 2020
Revised: Sep 18, 2020
Accepted: Sep 29, 2020

INTRODUCTION

The microtubule (MT) cytoskeleton is critical for establishing intracellular organization. During interphase, this network adopts the form of an astral array with MTs emanating from a central nucleating focus (centrosomes in animal cells) and branching outward throughout the cell. Importantly, the center of this aster is typically found near the geometric center of the cell, where it associates with the surface of the nuclear envelope. Forces generated by the MTs themselves move organelles during interphase, and because the network serves as a scaffold upon which these organelles attach and move, the aster's position dictates their spatial arrangement within the cell. During mitosis, spindle assembly is initiated in part by MT nucleation from centrosomes, and thus centrosome location at the interphase-to-mitosis transition has a role in determining where the spindle forms and in establishing the eventual location of the cell division plane (for a review, see McNally, 2013).

Although aster centering is likely to be critical in all cells, it is particularly relevant in large single-celled blastomeres immediately after fertilization. Here, the male pronucleus and its associated centrosome must traverse large distances to reach the cell center and establish the location of pronuclear fusion, spindle formation, and division plane positioning during the subsequent mitosis (e.g., Reinsch and Gonczy, 1998; Wuhr *et al.*, 2009). Thus, errors in this process can lead to erroneous cell division and have deleterious effects on developmental progression. Precisely how the MT aster generates and responds to forces to move to the cell center remains unanswered, in part because the most commonly used biological

This article was published online ahead of print in MBoC in Press (http://www.molbiolcell.org/cgi/doi/10.1091/mbc.E20-01-0088) on October 7, 2020.

*Address correspondence to: Jesse Gatlin (jgatlin@uwyo.edu).

Abbreviations used: aMTOC, artificial microtubule organizing center; CoMM, center of microtubule mass; MT, microtubule; PDMS, polydimethylsiloxane; PEGDA, poly (ethylene glycol) diacrylate; PEGdiPDA, poly (ethylene glycol) diphotodegradable acrylate.

model systems—large blastomeres from sea urchins (Minc *et al.*, 2011; Tanimoto *et al.*, 2016), *Caenorhabditis elegans* embryos (Gonczy *et al.*, 1999; Labbe *et al.*, 2004; Nguyen-Ngoc *et al.*, 2007), sand dollars (Rappaport and Rappaport, 1994), and *Xenopus laevis* (Wuhr *et al.*, 2009, 2010)—are intrinsically limited in terms of the shapes they can adopt (although some impressive work to manipulate shape has been done in these systems, e.g., Minc *et al.*, 2011; Chang *et al.*, 2014; Tanimoto *et al.*, 2016). With the notable exception of *C. elegans* embryos, the aforementioned model systems are also limited in terms of their genetic and biochemical tractability. Furthermore, although large cells are somewhat amenable to imaging, their thickness precludes live-cell imaging with a high signal-to-noise ratio that would allow for a more detailed characterization of the spatial and temporal dynamics of the MTs involved. Addressing these limitations will be important for advancing our current understanding of the MT cytoskeleton, including how it moves within the cell and how it organizes the cytoplasm.

Most studies addressing aster positioning have typically approached the phenomenon in one of two ways, either by using purely reconstituted systems confined to small wells in polydimethylsiloxane (PDMS) microfabricated chambers (Holy *et al.*, 1997; Dogterom *et al.*, 2005; Roth *et al.*, 2014) or by manipulating living blastomeres physically and/or biochemically (Kimura and Kimura, 2011; Minc *et al.*, 2011; Tanimoto *et al.*, 2016). These studies are complemented by theoretical descriptions and models of the process (e.g., Letort *et al.*, 2016; Nazockdast *et al.*, 2017). However, there still exists a need to differentiate between possible underlying biophysical mechanisms. Currently, there are three prevailing models used to describe how an aster can generate (or respond to) the forces necessary to move it from the edge of a large cell to the center of that cell, all of which are equally plausible and not mutually exclusive: cortical pulling, cortical pushing, and cytoplasmic pulling (Nazockdast *et al.*, 2017; Wu *et al.*, 2017).

In the cortical pulling model, minus end–directed motors that are bound to the cell cortex (e.g., cytoplasmic dynein) generate pulling forces on the plus ends of MTs as they interact with the cell cortex (Laan *et al.*, 2012a,b; Lammers and Markus, 2015). However, this model fails to adequately explain other experimental observations, including results from MT ablation/severing studies (Tanimoto *et al.*, 2016), ;which indicate that the nucleating center of the aster moves to follow the center of its MT mass (CoMM), a result more consistent with the cytoplasmic pulling model (see below). Additionally, in the context of aster positioning in large blastomeres, aster movement away from the proximal cortex begins before MTs reach the opposite side of the cell (Wuhr *et al.*, 2009, 2010), suggesting that other mechanisms are likely responsible, at least at the initial stages of aster movement away from a barrier.

Like the cortical pulling model, the cortical pushing model involves interactions between MTs and the cell cortex. In this case, however, the driving force is generated by polymerizing MT ends as they grow into the rigid "barrier" represented by the cell cortex. This model is supported by in vitro observations and measurements of forces generated by MT–barrier interactions (Holy *et al.*, 1997; Laan *et al.*, 2008) as well as by in vivo observations of MT buckling (Brangwynne *et al.*, 2006) and in small cells such as yeast and *Dictyostelium* (Tran *et al.*, 2001; Brito *et al.*, 2005). The validity of this model is undermined by the fact that the mechanical properties of individual MTs make them poor bearers of compressive loads and that the critical length of MT buckling is an order of magnitude or two shorter than the distances that asters traverse in large cells (Brangwynne *et al.*, 2006). However, the architecture and connectivity of the MT network within an aster, in terms of MT bundling and branching, could dramatically affect the length scale over which an aster could exert productive pushing forces against a barrier.

Finally, there is the cytoplasmic pulling model, which describes forces thought to be generated by the movement of cytoplasmic dynein (hereafter "dynein"), a minus end–directed MT motor, as it transports cargo from the peripheral cytoplasm toward the aster center (Kimura and Onami, 2005; Tanimoto *et al.*, 2016). As the dynein motors and associated cargoes move through the viscous cytoplasm, the drag force generated is countered by an equal and opposite force on the aster. When integrated over the entirety of the aster, these forces are sufficient to move the aster. This model predicts that force should be proportional to asymmetries in MT density (a proxy for motor density) and is supported by recent experimental observations of dynein-dependent aster motion in large blastomeres (Kimura and Kimura, 2011; Tanimoto *et al.*, 2016) and by compelling observations of aster movement in sea urchin embryos following induced aster asymmetry–during which the asters always moved away from the site of laser-induced MT ablation/severing (Tanimoto *et al.*, 2016).

Here we describe the application of a new approach engineered to overcome existing limitations inherent to earlier methods and to investigate the biophysics of aster movement and centration in large cells. It combines PDMS microfluidic devices, photolabile hydrogels, *X. laevis* egg extract (Desai *et al.*, 1999; Maresca and Heald, 2006; Good and Heald, 2018), and confocal microscopy to resolve the mechanics of aster movement in a tractable, cell-free system that closely resembles the cytoplasm within a cell (Parsons and Salmon, 1997; Desai *et al.*, 1999). Using this approach, our observations of aster movement and centration in confining geometries suggest that MT-dependent pushing forces are sufficient to move asters over the length scales explored and that the arrangement of MTs within the aster is capable of bearing the resulting compressive loads.

RESULTS

Aster centration in PDMS channels does not require dynein activity

To investigate the mechanics of aster centration in a way that allows greater flexibility in exploring the effects of enclosure geometry, we confined *X. laevis* egg extract containing artificial microtubule-organizing centers (aMTOCs) in either PDMS walled channels (Figure 1, A and B; Supplemental Videos 1 and 2, respectively) or annular cylinder hydrogel enclosures within larger PDMS channels (Figure 1C; Supplemental Video 3) and monitored their position over time using time-lapse spinning-disk microscopy. The poly(ethylene glycol)-based hydrogels used in these experiments have proven to be compatible with *X. laevis* egg extracts (Supplemental Figures S1 and S2; Bisht *et al.*, 2019; Geisterfer *et al.*, 2020) and exhibit low levels of nonspecific protein binding to their surfaces (Nuttelman *et al.*, 2001; LeValley *et al.*, 2018). We also note that our extracts contained cytochalasin D (10 μg/ml (Desai *et al.*, 1999), which is routinely added during preparation to disrupt the formation of filamentous actin and inhibit gelation and contraction of the extract (Field *et al.*, 2014). As such, the physical properties of the extracts used here likely differ from those found in vivo. MTs were visualized by supplementing egg extract with an engineered fluorescent MT-binding protein (mCherry-TMBD; Mooney *et al.*, 2017). This visualization strategy was chosen because these tau-based constructs confer a higher signal-to-noise ratio compared with traditional MT-labeling approaches using fluorescent tubulin and have been shown to only minimally affect MT dynamics (Mooney *et al.*, 2017; Field *et al.*, 2019; see also Supplemental Figures S1 and S2).

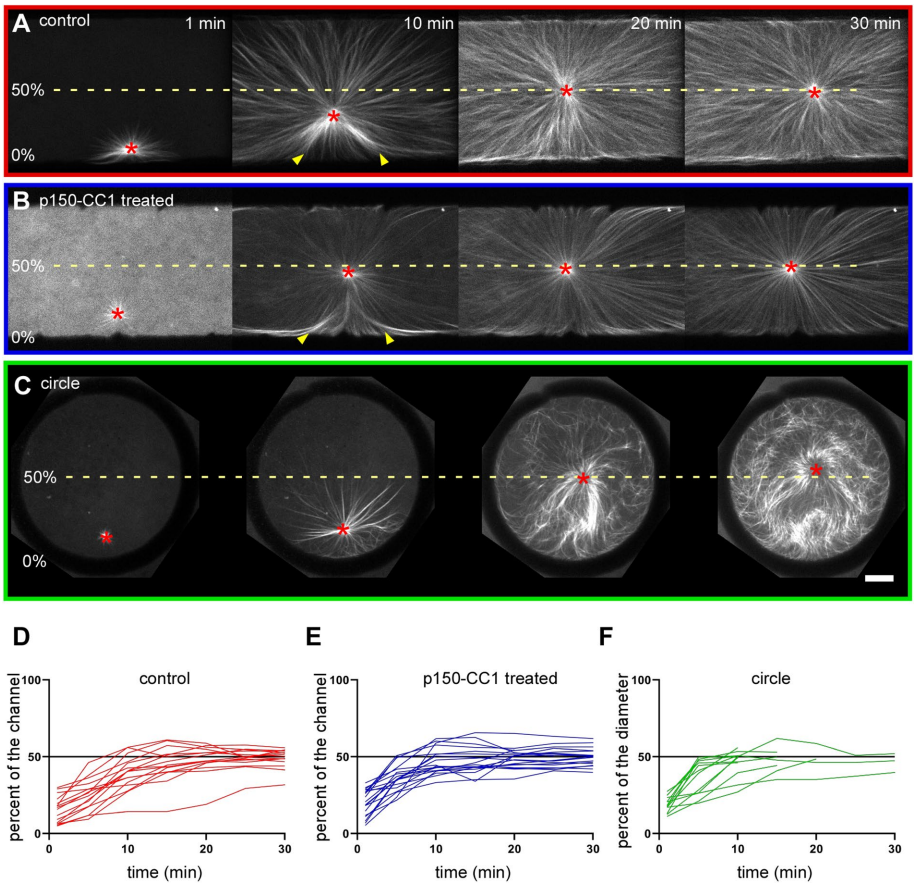

FIGURE 1: Dynein inhibition via addition of p150-CC1 does not affect aster centration in *X. laevis* egg extracts. Centration of aMTOCs in interphase *X. laevis* egg extracts was investigated in PDMS microfluidic channels or hydrogel annular cylinders. Time-lapse spinning-disk confocal microscopy was used to visualize MTs, which were labeled with mCherry-TMBD and are shown in grayscale (A–C). The dashed line in each series of images runs through the midpoint of the channel width (A, B) or the center of the annular cylinder (C) and represents 50% of the channel width or interior diameter accordingly. Images in A show an aster starting near a PDMS channel wall (0%) and centering over time in untreated extract, whereas the images in B show similar aster centration in extract treated with 2 μM p150-CC1. Images in C show aster centration within a hydrogel annular cylinder in untreated extract. For each experimental condition, the aMTOC position (red asterisk) relative to the proximal wall was plotted over time as a percent of the channel width in D (red lines) and E (blue lines) and of the interior diameter in F (green lines). The colored lines represent traces from each individual experiment; $n \geq 10$ for each condition. Yellow arrowheads point to MT bending. For all images, scale bar = 20 μm.

To determine whether we could recapitulate in vivo aster centration as it occurs in large blastomeres (~100 μm in diameter; Minc *et al.*, 2011; Tanimoto *et al.*, 2016), we first flowed extract containing aMTOCs into PDMS devices containing arrays of channels that were ~1 mm in length, ~100 ± 10 μm in width, and ~30 μm in height. Filled devices were kept on ice until being placed on the microscope stage to prevent MT polymerization and movement of aMTOCs. To normalize for the slight variation in channel width among devices, aster movement was tracked as a percentage of channel width, with 0% representing the nearest wall and 50% representing the center of the channel. Only aMTOCs that were within 30% of the nearest wall at experimental onset were tracked. We found that asters in channels were able to center, on average, within ~20 min and, once centered, tended to maintain their position within the channel (Figure 1, A and D). We also observed MTs fanning out along the proximal wall, which we attribute to some MTs slipping along the surface as they grow. aMTOC asters confined within a more cell-like geometry of annular cylinders made of poly(ethylene glycol) diacrylate (PEGDA) hydrogels with diameters of ~100 μm also centered and did so with similar velocities as compared with asters in PDMS channels (Figure 1, C and F; Supplemental Figure S3). These data suggest that the underlying mechanism was largely unaffected by the specific composition of the barrier surfaces and that the underlying forces were capable of centering asters over the length scales tested, ~50 μm, or half the width of our channels and half the diameter of our annular enclosures.

To begin to elucidate the nature of the forces responsible for centration and to differentiate more broadly between a MT-dependent pushing mechanism and one that involves dynein-dependent pulling, we compared the dynamics of aster centration in PDMS channels in the presence and absence of the dynein inhibitor p150-CC1 (2 μM; Gaetz and Kapoor, 2004). When added to spindle assembly reactions in mitotic extracts, this treatment resulted in the well-established "haystack" spindle phenotype (Mitchison *et al.*, 2005; Gatlin *et al.*, 2009). This phenotype was also observed in assembly reactions within PDMS channels containing hydrogel structures and in the presence of mCherry-TMBD to visualize MTs (Supplemental Figure S1), suggesting that the reagents used in our studies, as well as the binding of mCherry-TMBD to MTs, likely did not interfere with p150-CC1–mediated dynein inhibition. The same treatment also resulted in a failure of membrane accumulation near the aster center (Supplemental Figure S1B), as observed previously (Hara and Merten, 2015; Cheng and Ferrell, 2019). Taken as a whole, these data suggest that our experimental approach had little effect on the ability of p150-CC1 to inhibit dynein. Interestingly, and in contrast to previous reports in which aster centration was negatively affected after dynein inhibition using ciliobrevin (Tanimoto *et al.*, 2016, 2018; Cheng and Ferrell, 2019), dynein inhibition using p150-CC1 had no noticeable effect on aster centration in our studies (Figure 1, B and E). These data suggest that the centering mechanism used under our experimental conditions does not require the activity of dynein. We note, however, that previous studies have shown that aster centration in *X. laevis* embryos is indeed sensitive to p150-CC1 treatment (Wuhr *et al.*, 2010), an apparent conflict that we address in the *Discussion*.

Aster centration can be disrupted using asymmetric hydrogel structures

We next investigated whether aster centration in extracts can be affected by aster asymmetries induced by the geometry of the confining enclosures. Both the cytoplasmic pulling and the cortical pushing models rely on asymmetries in the aster to induce motion.

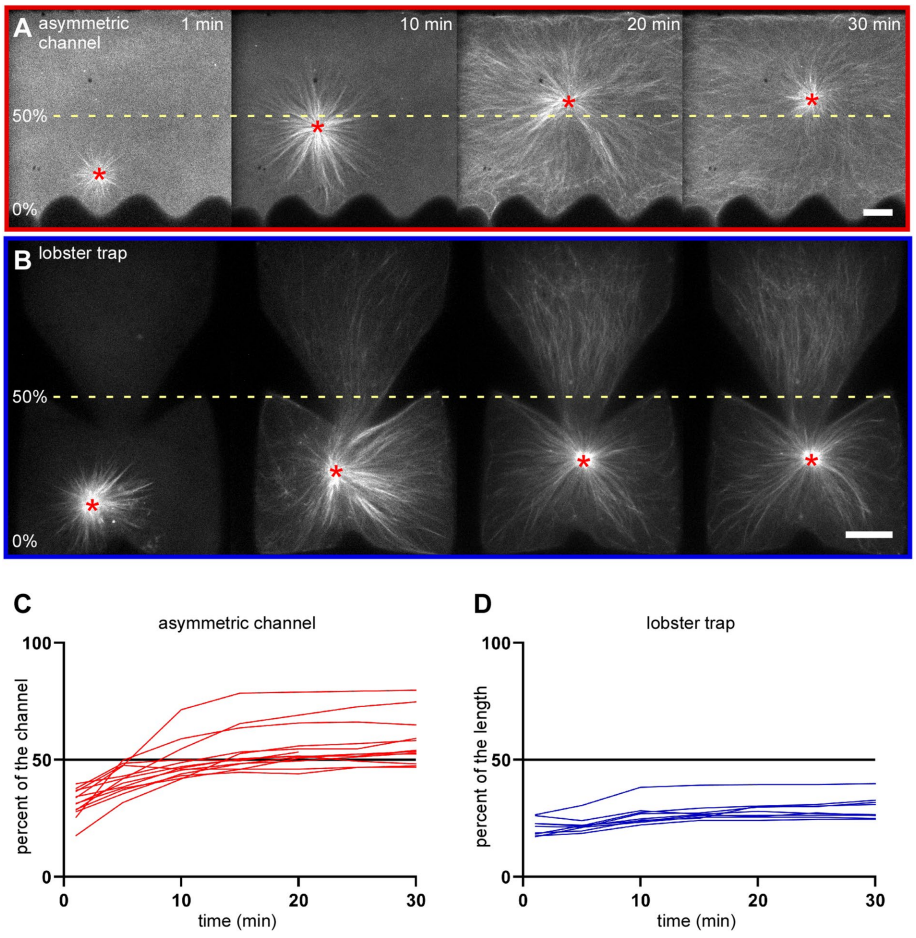

FIGURE 2: Asters are unable to center when confined in certain asymmetric enclosure geometries. The ability of aMTOC asters to center was investigated in asymmetric microfluidic channels (A) and asymmetric hydrogel structures designed to resemble the cross-section of the inside of a lobster trap (B). Aster movement was visualized and tracked as described in Figure 1. For each set of time-lapse image series, the dashed yellow lines run through the midpoint of the asymmetric channel width (A) or the center of the lobster trap enclosure (B) and represent 50% of the channel width or interior length, respectively. For the experimental conditions shown in A and B, the aMTOC position (red asterisk) relative to the nearest wall at experimental onset was plotted over time as a percent of the channel width and interior length with the graphs in C (red lines) and D (blue lines), respectively. The colored lines represent individual traces for each experiment; $n \geq 9$ for each condition. For all images, scale bars = 20 μm.

For the cytoplasmic pulling model, it is asymmetry in the aster itself that generates the force in the direction of the geometric center. In contrast, for a pushing-based model it is an asymmetry in position that causes force to be directed away from a proximal barrier. On the basis of observations of aster shape in our smooth-walled PDMS channels, specifically the fanning-out of MTs along the proximal wall (e.g., Figure 1A, 10-min image), we posited that MT ends might impact the wall and then slide along it. Indeed, we observed slipping of EB1-GFP–labeled MT ends as they grew into hydrogel barriers (Supplemental Figure S4). In these experiments, the tendency of growing MT ends to slip and grow along the barrier seemed to increase as the contact angle with the barrier became more acute. We reasoned that slipping ends, if unable to gain purchase, would produce less pushing force against the barrier. Therefore, if we could mitigate this slipping, we could affect aster centering. To test this hypothesis, we generated channels in which one wall was smooth and the other was sawtoothed, with peaks and troughs designed to reduce MT slippage on one side of the channel (see *Materials and Methods*; Figure 2A; Supplemental Video 4) We defined the midpoint of these asymmetric channels as the point located halfway between a line running parallel to the channel wall and through the geometric center of the sawtooth peaks (and troughs) and the opposite PDMS wall. This yielded devices with an average width of 100 ± 20 μm. As in Figure 1, channel widths were normalized to account for variation, and aster movement was tracked as a percentage, with 50% corresponding to the channel midpoint (Figure 2A). Only aMTOCs whose starting positions were closest to the sawtooth side of the channel were tracked. Several asters were able to move beyond the channel midpoint and achieve a steady state position farther away from the sawtooth side of the channel and closer to the smooth side, resulting in a noticeable increase in the average deviation from the channel center as compared with the symmetric controls (Figure 2, A and C; Supplemental Figure S3). This observation suggests that a net force, directed away from the sawtooth wall, is applied to the aMTOC at the channel midpoint and is consistent with the idea that growing MT ends can more easily gain purchase on the sawtooth wall.

One way to define aster asymmetry is to calculate the distance between a point representing the nucleating center of the aster, in our case the aMTOC, and another representing the center of mass of all aster MTs (referred to as the CoMM). For cytoplasmic pulling models, the larger the separation between these two points, the larger the degree of aster asymmetry and, in theory, the larger the net centering force. In the absence of other types of forces, the net centering force produced by pulling against the cytoplasm should approach zero as these two points converge. As such, if a confined aster could achieve a steady state position in which its nucleating center (or aMTOC) and its CoMM are spatially separated, it would suggest that other types of forces are at play, for example, a countering pushing force. To test this hypothesis, we challenged aster centering within enclosures of a more complex geometry, one that resembles the cross-sectional area of a traditional lobster trap (Figure 2B; Supplemental Video 5). By design, the geometric center of these enclosures lies outside of the bottom chamber of the trap (as oriented in Figure 2), near the 50% midpoint of the trap's long axis (~130 μm in length). aMTOCs were initially positioned in the bottom chamber (or in the trap) and their position tracked over time as they nucleated MTs, formed asters, and moved. The position of each aMTOC was graphed as a percent of the length of travel along this long axis (Figure 2D). We found that asters were, without exception, unable to exit the trap and reach the geometric center of the enclosure. Instead, they seemed to reach an equilibrium position near the geometric center of the bottom chamber. This is despite

aster MTs extending throughout the entirety of the enclosure, making the position of the geometric center of the enclosure and that of the aster CoMM the same. We argue that the inability of aMTOCs to migrate to the geometric center of these enclosures (and, by extension, to the CoMM of the aster) suggests that a cytoplasmic pulling mechanism is not solely responsible for aster movement and centering in this system.

Aster movement away from V-shaped hydrogel barriers supports a pushing-based mechanism

To further elucidate the force mechanism(s) responsible for generating aster movement and centration, we investigated the impacts of aster proximity to a wall and of induced aster asymmetry on aster movement. To address this experimentally, aMTOCs were transiently captured in small degradable hydrogel cylinders composed of poly(ethylene glycol)di-photodegradable acrylate (PEGdiPDA), a photolabile polymer derivative of PEGDA (Kloxin *et al.*, 2009). The unpolymerized PEGdiPDA was then washed out of the microfluidic device and replaced with PEGDA to generate photostable hydrogel barriers near the PEGdiDPA-encapsulated aMTOCs. The end result was an encapsulated aMTOC positioned at the vertex of a V-shaped PEGDA hydrogel barrier with either a 30° or a 90° interior angle (Figure 3A). After unpolymerized PEDGA solution was washed out of the device and replaced with interphase egg extract, the PEGdiPDA cylinder encasing the aMTOC was degraded via exposure to 365-nm UV light, thereby releasing the aMTOC and allowing it to begin nucleating MTs. At this point in the experiment, we began tracking aMTOC motion away from the vertex as a function of time. In contrast to the previous experiments (shown in Figure 1) in which aMTOCs were initially free and positioned somewhat randomly at experimental onset, this approach allowed us to synchronize the starting position and afforded exquisite control over the initial position of the aster as well as the timing of movement onset.

V-shaped barriers with interior angles of 30° (30°V) and 90° (90°V) were used in these experiments. The specific barrier shape was chosen because it forced the expanding MT network to adopt an asymmetric morphology, being constricted on the side closest to the vertex and more expansive on the open side of the V. These hydrogel structures were made near the middle of large channels (~1 cm long, 1 mm wide, and 30 µm high) within our PDMS devices, typically hundreds of microns away from each other or any vertical PDMS wall. By varying the angle of the V, we ensured that the aMTOC would always be closer to a barrier in the more acute 30°V as compared with the more obtuse 90°V (see Figure 3, B and C, respectively). For both geometries, released aMTOCs nucleated MTs and began to move away from the vertex along a horizontal line centered on the V with very little deviation from the center of the V (Figure 3, B and C; Supplemental Videos 6 and 7). The distance traveled along this line was plotted as a function of time for each geometry (Figure 3D). On average, the aMTOCs in the 30°V moved faster and farther from the vertex than those in the 90°V.

If modeled as a beam, as MTs push against a barrier the force they can exert before buckling is proportional to $1/(\text{MT length})^2$. Because the aMTOC is always closer to a barrier wall in the 30°V than in the 90°V at the same distance away from the vertex, if pushing is the responsible mechanism, the force exerted on the aMTOC in the 30°V will be larger than that experienced in the 90°V, perhaps explaining the difference in observed aMTOC velocities (Figure 3D). Indeed, MTs are capable of polymerizing against a hydrogel barrier in our system, based on observations of the interactions between growing MT ends and barriers (Supplemental Figure S4). In contrast to MT pushing models, cytoplasmic pulling models predict that aMTOC velocity should be proportional to the distance between the aMTOC and the aster's CoMM (see *Materials and Methods*) and should be directed along the line connecting the two. To attempt to differentiate between these two models, "instantaneous" aMTOC velocities were calculated by taking the slopes of the distance-versus-time plots in Figure 3D at 5-min intervals and plotting them against either 1) proximity to the nearest wall, as determined geometrically (Figure 3E) or 2) the distance between the position of the aMTOC and the aster's CoMM (Figure 3F). In these plots, positive velocity values were assigned to aMTOC movement away from the vertex (left to right as depicted in Figure 3). In both the 30°V and 90°V barriers, velocities were higher closer to a barrier and dropped off as the aster moved farther away from the vertex, consistent with a pushing model. We found that this relationship held constant for all experimental conditions tested (Supplemental Figure S3). Interestingly, we found that the highest aMTOC velocities correlated with negative distances between the aMTOC and aster CoMM, meaning that aMTOCs moved away from the vertex faster when more MTs were present between the aMTOC and the vertex than were in front of the aMTOC. Particularly at later time points, these geometries produced the expected aster asymmetry, reflected by spatial separations between the positions of the aMTOC and the aster CoMM (Figure 3F). When these spatial separations were plotted versus the instantaneous aster velocity (Figure 3F), we found a negative correlation between the two parameters. This observation suggests that a pulling-based mechanism cannot be solely responsible for aster movement away from a barrier.

Decoupling aster growth from aster movement suggests that bulk translocation of the entire aMTOC-associated MT network is not required for aster centration

Current models of aster centration (both pushing and pulling based) implicitly require bulk translocation of the entire aster MT network as it moves through cytoplasmic space en route to the cell center. Whether this assumption is truly valid remains unaddressed, in part because asters in vivo are typically expanding while they move and achieve centration only coincident with expansion throughout the entirety of the confining cell. The question remains as to whether an aster's nucleating center can find the center of an enclosed space without bulk translocation of the entire aster MT network, and indeed, recent experimental evidence suggests that this might be the case. For example, a recent in vitro study suggested that asters can simply assemble de novo in confined volumes and effectively center themselves without translocation (Juniper *et al.*, 2018). Additionally, nuclei, and presumably their surface-associated centrosomes, seem to be able to move independently of asters that form in the tessellated compartments of cycling extracts (Cheng and Ferrell, 2019). To determine whether aMTOCs can find the center of enclosures when aster movement is decoupled from aster growth, we used a modified version of the method outlined in Figure 3A, in which the aMTOC was only partially embedded in a temporary PEGdiPDA cylinder (Figure 4A). This allowed the aMTOC to nucleate MTs from its extract-exposed surface while preventing its movement until it was released by photo-induced degradation of the cylinder. Additionally, the electronic mask used originally for the 30°V experiments (Figure 3B) was altered to generate a V with a capped end to form a teardrop-shaped enclosed volume (Figure 4, A, C, and D; Supplemental Videos 8 and 9). Confining the aster in this way also let us test a fundamental prediction of the pushing model, that longer MTs on the leading side of the aMTOC would generate less force, due to the length dependence of buckling, than shorter MTs on the lagging side of the aMTOC. To determine whether aMTOCs could center in

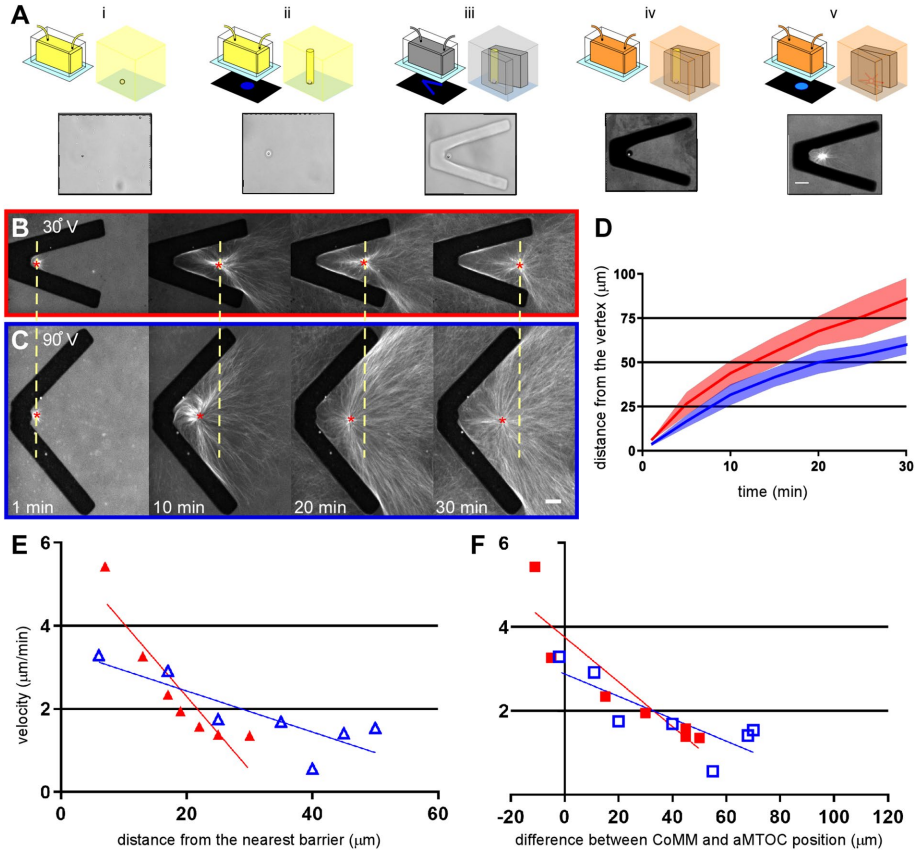

FIGURE 3: Aster movement away from V-shaped barriers implies a pushing-based mechanism for translocation. Each of the paired sets of cartoon depictions in the top row of A shows a microfluidic device (left) and a zoomed-in view of the channel interior (right) for the different steps required for aMTOC capture and V-shaped structure formation. Corresponding bright-field and fluorescent images of each sequential step, moving left to right, are shown in the bottom row. (i) A photolabile prepolymer hydrogel solution (PEGdiPDA) containing aMTOCs was flowed into the channel of a microfluidic device. (ii) The hydrogel solution was exposed to UV light ($\lambda = 405$ nm) patterned using a digital micromirror array placed in a conjugate plane to the specimen in the light path of the microscope. For these experiments, a small circle in the electronic mask was aligned with an aMTOC in the PEGdiPDA solution. Upon exposure, this produced a cylindrical column of photolabile hydrogel surrounding an aMTOC at its base, temporarily fixing it in place and preventing the aMTOC from being washed away in subsequent steps. This anchoring step was repeated for multiple aMTOCs in the prepolymer solution. (iii) A nondegradable prepolymer hydrogel solution (PEGDA) was flowed into and exposed to UV light ($\lambda = 405$ nm) in the shape of a V aligned such that the aMTOC being targeted was positioned close to the vertex of the hydrogel structure. (iv) After the generation of all structures, the unpolymerized solution within the device was washed out with buffer and ultimately replaced with interphase *X. laevis* egg extract. (v) The aMTOC was released by degrading the PEG-diPDA cylinder with exposure to higher-energy UV light ($\lambda = 365$ nm). Extracts were supplemented with mCherry-TMBD, and aMTOC aster movement was recorded using time-lapse spinning-disk confocal microscopy as in Figure 1. An example of aster movement from the vertex of a 30°V is shown in B and from a 90°V in C. The yellow dashed line in each image extends from the center of the aMTOC position (red asterisk) in B and is included to facilitate comparison of aMTOC velocity away from the vertex in C. aMTOC movement away from the vertex of the 30°V (average position, red line) and 90°V (average position, blue line) structures was plotted as a function of time to make the graphs shown in D. Shaded outlines represent 95% confidence intervals; $n \geq 10$ for each V type. Using the slopes from these plots, the aMTOC instantaneous velocity was plotted vs. the shortest distance to the nearest barrier surface (E) and the distance between the CoMM (see *Materials and Methods*) and the aMTOC (F) for both 30°V (filled red triangles and squares, respectively) and 90°V (open blue triangles and squares, respectively) structures. Here a positive velocity indicates that the aMTOC was moving away from the vertex. For all images, scale bars = 20 μm.

teardrop enclosures and establish a baseline behavior for coupled aster growth and aster movement, we tracked the movement of aMTOCs from the vertex of the teardrops and plotted aMTOC position as a function of time (Figure 4, C and F). Results from coupled experiments conducted using open 30°V barriers (taken from Figure 3A) are included for comparison (Figure 4, B and E). We observed similar aMTOC movement behaviors in coupled experiments for both the open 30°V (Figure 4, B and E) and the enclosed teardrops (Figure 4, C and F). For the uncoupled condition (Figure 4, D and G), aMTOCs were permitted to nucleate MTs until the network had expanded to fill the interior of the teardrop for ~15 min, after which the aMTOCs were released and tracked. Immediate movement of the released aMTOCs suggested that they were able to move away from the vertex and through the preexisting MT network, albeit not quite as fast or as far as compared with the other experimental conditions. These observations suggest that the aMTOC can move independently from the bulk MT network. We also observed MT bending in front of the moving aMTOCs (Figure 4, white arrowheads), suggesting that the filaments were under a compressive load and unable to oppose the larger pushing forces generated by shorter growing MTs behind the aMTOC.

DISCUSSION

Our results implicate a pushing-based force generation mechanism as playing a larger role in aster movement and centration than previously acknowledged and one that could be the predominant mechanism underlying aster movements within large cells, at least on a scale of ~100 μm or less in diameter. We found that aMTOC-nucleated asters can indeed find the center of PDMS channels as well as annular cylinder hydrogel enclosures, suggesting that our model system might serve as a reasonable proxy to study the phenomenon. In agreement with recent published studies in sea urchin embryos, (Meaders *et al.*, 2020), inhibition of dynein via p150-CC1 did not affect aster centration in our extracts. Taken at face value, this would suggest that aster centration, over the length scales tested, can occur independently of dynein function and would implicitly rule out a dynein-dependent pulling-based mechanism. However, this result contradicts observations of the effects of dynein inhibition on aster centration over similar length scales in vivo. Specifically, in large sea urchin blastomeres (~100 μm in diameter), treatment with the dynein inhibitor ciliobrevin was shown to negatively affect aster centration (Tanimoto *et al.*, 2016). p150-CC1 injection into *X. laevis* embryos (~1.2 mm in diameter) resulted in asters that failed to reach the cell center after traveling ~200 μm from the blastomere cortex, suggesting that dynein activity is not

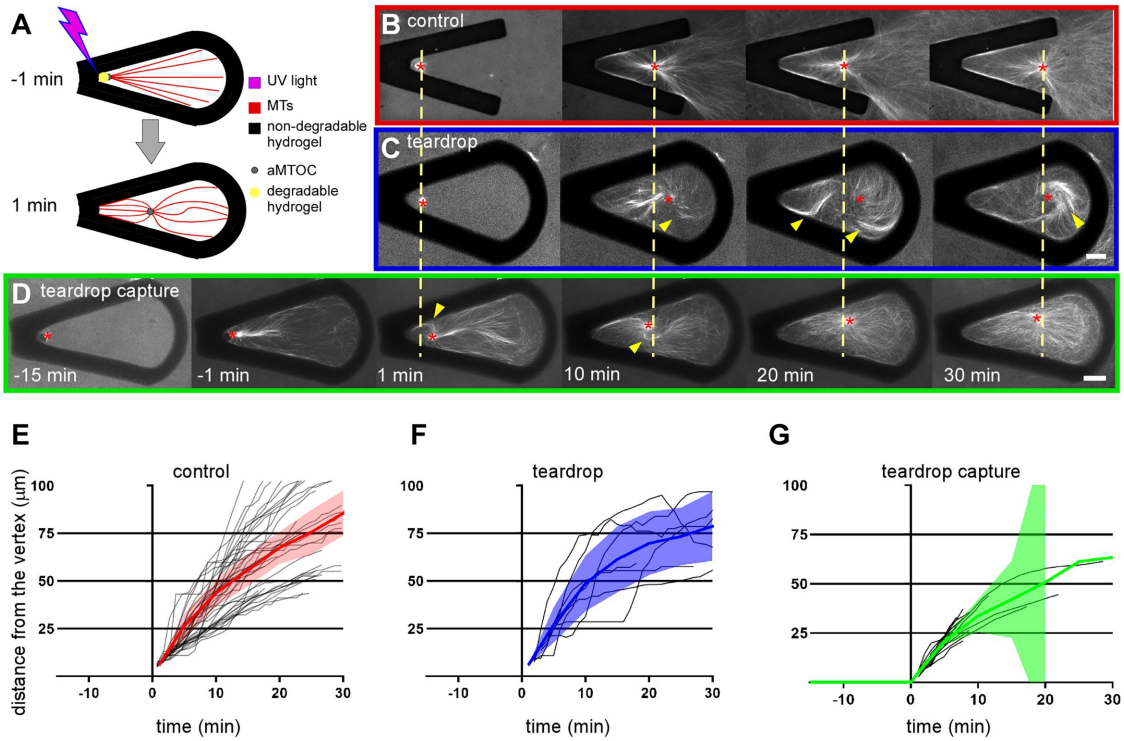

FIGURE 4: Aster movement does not require bulk translocation of the entire MT network. The cartoon in A illustrates the approach used to decouple aster growth and aMTOC movement. aMTOCs were partially embedded in PEGdiPDA posts using the methodology described in Figure 3A such that they could nucleate MTs from their extract-exposed surfaces before being released. Time-lapse spinning-disk confocal microscopy was used to visualize MTs labeled with mCherry-TMBD as in Figure 1. The yellow dashed line at each time point in B extends from the aMTOC position (red asterisk) and is included to facilitate comparison of aMTOC velocities after release at time = 0. The images in B and C show aMTOC movement at the start of nucleation away from the vertex of a 30°V and a 30° teardrop, respectively. In contrast, the images in D show an aMTOC only partially embedded in the PEGdiPDA post and allowed to nucleate MTs for 15 min before light-induced release as described in A. For each experimental condition, aMTOC movement away from the barrier's vertex was plotted as a function of time with positional data from B, C, and D shown in graphs E, F, and G, respectively. Shaded outlines represent 95% confidence intervals; gray lines represent each experiment; $n \geq 6$. Yellow arrowheads point to MT bending. For all images, scale bars = 20 μm.

required for aster movement over shorter length scales but might be required for translocation over longer distances (Wuhr *et al.*, 2010). Even in *Xenopus* egg extracts, dynein inhibition (via ciliobrevin and p150-CC1, respectively) affects both MT aster-dependent compartmentalization (Cheng and Ferrell, 2019) and aster–aster separation in bulk *X. laevis* egg extracts (Pelletier *et al.*, 2020). In the context of a pushing-versus-pulling argument, we should emphasize that we used PEGDA and PDMS barriers in our in vitro experimental approach. Characterization of the architectures of asters grown on slabs made of these materials and the observed MT slipping as shown in Figure 1 suggests that they are largely inert in terms of motor binding, a conclusion that is also supported by the observation of slipping of MT growing ends along vertical barriers (Supplemental Figures S2 and S4). Thus, it is unlikely that motors anchored at the barriers mediate cortical pulling, though it is abundantly clear that this mechanism is involved in spindle centration in vivo (Aist *et al.*, 1993; Adames and Cooper, 2000; Labbe *et al.*, 2004; Park and Rose, 2008; Kotak *et al.*, 2012; Okumura *et al.*, 2018). Taken as a whole, these data suggest that it is possible for MT-dependent pushing forces to center asters in cells up to ~100 μm in diameter.

The observation that aMTOC asters failed to reach the geometric center of our lobster trap enclosures and instead adopted a decentered final position in which the aMTOC was not spatially coincident with the aster CoMM is consistent with a force contribution from a pushing-based mechanism and implicitly argues against a model that relies solely on cytoplasmic pulling, which would predict that the aster would indeed be able reach the geometric center. We propose that this failure to center is caused by the collection and focusing of growing MTs into the triangular recesses on either side of the trap's constriction and by the resultant generation of pushing forces that work to keep the aster in the lower chamber of the trap. This argument requires that MTs continue to grow once they hit a hydrogel barrier and is supported by our observation that when EB1-decorated growing ends (comets) encounter a hydrogel barrier, they indeed continue to grow and will either remain at the point of impact or slide along the barrier. depending on the angle of contact (Figure 1A; Supplemental Figure S4). The same logic could be applied to explain the results of experiments in sawtooth channels, in which asters reached equilibrium positions farther away, on average, from the sawtooth side of the channel, consistent with the idea that pushing forces against the channel walls were uneven and were made more productive by the sawtooth geometry. We acknowledge that the results from our lobster trap experiments do not definitively rule out the possibility that pulling forces are still at play and that aster centration is prevented in these channels not by a pushing mechanism, but instead by steric constraints imposed by the physical properties of the aster, that is, the aster is simply too large and too rigid to be pulled through the constriction. Recent

characterizations of aster dynamics in F-actin–intact egg extracts indeed suggest that these assemblies behave as elastic, deformable gels (Pelletier *et al.*, 2020). However, we argue that if pulling forces play a predominant role in centration, the dynamic nature of aster MTs should still allow the aster to reorganize around the constriction over time and ultimately reach the center of these devices. Clearly, more work needs to be done to measure the mechanical properties of the aster as a whole.

Our observations of aMTOC movements away from V-shaped hydrogel barriers make a compelling case for a pushing-based mechanism. This geometry provides little opportunity for motors to anchor to the barrier in a way that would allow for the aster behavior that we observed. We are confident that our PEGDA hydrogels are relatively inert and minimize the potential for nonspecific protein binding (Nuttelman *et al.*, 2001; LeValley *et al.*, 2018). As the asters always moved out of the V-shaped barriers toward the opening, this suggests that cortical pulling is likely not a major contributor to the phenomenon. The aMTOC velocity was higher and they moved farther from the vertex in 30°V barriers, a geometry that allowed for closer proximity to the wall and potentially larger pushing forces to be generated, relative to similar experiments using 90°V barriers. Additionally, the relationship between velocity and aster asymmetry deviated from what one would expect if a cytoplasmic pulling mechanism was responsible, that is, a positive correlation between velocity and the separation distance between the aMTOC and the aster CoMM, which was up to ~70 µm with the V-shaped barriers. We instead observed a negative correlation, which we posit is likely the result of a combination of reduced pushing forces due to an increasingly larger separation between the aMTOC and nearest barrier and of a concomitant increase in resistive drag as the aster grows. Finally, we observed aMTOC movement away from barriers even when the aster CoMM was behind the moving aMTOC, which is most consistent with a pushing-based mechanism.

The compressive force that a single MT can bear or exert is thought to fall off as a function of 1/(MT length^2) according to the Euler buckling theory (Dogterom and Yurke, 1997; Kimura and Onami, 2005). Studies in vitro and mathematical modeling of single MTs suggest that the maximum force a single MT can exert before buckling is on the order of 3–10 pN and occurs at lengths of ~15 µm (Dogterom and Yurke, 1997; Holy *et al.*, 1997; Zhu *et al.*, 2010), far too short to account for the distances traveled by asters in our system and in the living blastomeres of specific echinoderms (Minc *et al.*, 2011; Tanimoto *et al.*, 2016) and amphibians (Wuhr *et al.*, 2009). It should be noted, however, that studies of MT bending modes in cells (Brangwynne *et al.*, 2006) suggest that MTs can withstand much larger compressive loads than predicted by in vitro observations. This line of reasoning and the negative effects of ciliobrevin treatment on aster migration (Tanimoto *et al.*, 2016) have led many researchers to discount pushing as a possible mechanism. We argue that a branched MT network might allow for pushing forces to act over longer distances. Indeed, the relatively constant density of growing MT ends in expanding asters (Ishihara *et al.*, 2014, 2016), coupled with MT-dependent MT nucleation (Petry *et al.*, 2013), is consistent with the idea that the distance between the aMTOC and a barrier is bridged by a tiled array of interconnected and short MTs, not by long MTs spanning the entire distance (Figure 5). Similarly, MT minus ends are distributed throughout meiotic monopoles in *X. laevis* extracts (Decker *et al.*, 2018). An interconnected network of MTs is likely better able to bear a compressive load, but its ability to do so is still dependent on the length over which the compressive load is borne. Indeed, following aster release in teardrop enclosures, the longer MT network on the leading side of the aMTOC

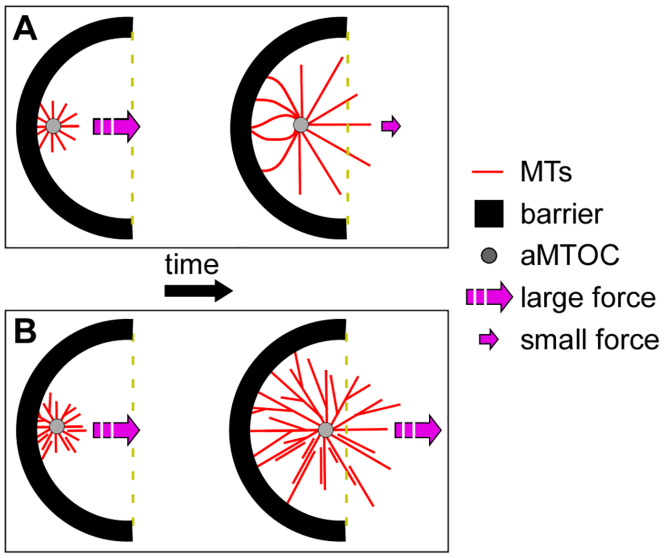

FIGURE 5: Cartoon summary for how MT-based pushing forces might facilitate aster movement in our system. The cartoon in A depicts how asters might behave assuming an unbranched, radial elongation model of aster growth. Initially, short unbundled MTs extending from the aMTOC and reaching the proximal barrier surface might be able to generate sufficient force to produce aster movement. However, later in time, once MTs approach their critical length, they would buckle under compressive loads, resulting in reduced force generation and a failure to center (dashed yellow line). The cartoon in B shows an architecturally more complicated aster with MT branching and bundling to effectively brace MTs and allow for more growing ends to impinge on the proximal barrier surface. In this model, MTs would be sufficiently buttressed by interactions with other MTs, resulting in a larger pushing force and, ultimately, a longer distance through which asters could traverse.

seemed prone to buckling, whereas the shorter MT network on the lagging side seemed less so. Regardless, more work has to be done to characterize the changes in MT dynamics and network organization that likely accompany aster movement and centration. Indeed, our observations that aster movement can be decoupled from aster MT growth suggest that some degree of structural independence is present within the aster. Recent experimental evidence suggests that this is indeed the case, as nuclei and associated centrosomes have been shown to center in tessellated arrays of MT asters formed in cycling extracts (Cheng and Ferrell, 2019).

So, how would we characterize our system, and what exactly is it telling us about aster centration? We like to think that the model system used here, cell-free extracts derived from frog eggs, lies somewhere on the continuum between in vitro and in vivo (but is closer to the in vivo end of the spectrum). Despite the fact that many fundamental mechanisms elucidated using *Xenopus* egg extracts have proven to be conserved, we acknowledge that this is indeed not an in vivo system. Furthermore, we note that we are also confining extracts and asters within artificial enclosures that most certainly fail to accurately mimic the plasma membrane in terms of its mechanical, biochemical, and geometrical properties. Therefore, many forms of regulation or feedback on MT dynamics that the plasma membrane normally confers in vivo are likely missing from our system. We also acknowledge that egg extract is not a true mitotic system. For all of the aforementioned reasons, we suggest using caution when extending our findings to explain aster and spindle positioning as it occurs in cells in vivo. Indeed, it is well established

that cortical pulling forces play a major role in aster/spindle positioning in several eukaryotic systems (for excellent reviews, see Kotak and Gonczy, 2013; McNally, 2013; Meaders and Burgess, 2020). Furthermore, data in support of the cytoplasmic pulling model, which are largely based on observations of aster and spindle positioning in sea urchin and in *C. elegans* blastomeres, are compelling (Hyman, 1989; Gonczy *et al.*, 1999; Kimura and Onami, 2005; Kimura and Kimura, 2011; Tanimoto *et al.*, 2016, 2018). For example, in sea urchins, inducing a rapid aster asymmetry via laser ablation of MTs on one side of an aster results in the aster moving away from the site of ablation, an observation consistent with a pulling mechanism but difficult to reconcile with cortical pushing. In these same model systems, inhibition of dynein (via treatment with ciliobrevin; Tanimoto *et al.*, 2016, 2018) inhibits the ability of asters to center, broadly implicating a pulling-based mechanism. Even in *X. laevis* egg extracts, the centration of individual nuclei—and presumably their associated centrosomes—within each tessellated tile formed by an aster, is abrogated upon treatment with ciliobrevin (Cheng and Ferrell, 2019; Field *et al.*, 2019). Finally, when comparing our centration dynamics to those that occur in *X. laevis* embryos, there are clear differences as well. The velocities observed in this system (~3–5 µm/min) are noticeably lower than those measured in vivo (~7 µm/min; Wuhr *et al.*, 2009). Furthermore, aster centration in single-celled *X. laevis* embryos requires dynein, but in this system the aster center has to travel upward of 600 µm to reach the cell center. Interestingly, even in embryos treated with p150-CC1, asters were able to move at least 200 µm away from the cortex (Wuhr *et al.*, 2010). This would suggest that there is a limit to how far asters can generate a productive pushing force and that aster movement beyond this point likely requires another mechanism.

In summary, the current state of the field leaves room for debate and, collectively, requires better approaches to provide more definitive answers. We believe that our data, taken as a whole, suggest that a pushing-based force mechanism is capable of moving an aster through cytoplasm and that these forces can act over longer-than-expected distances in the in vitro system used here. Whether the same mechanism functions in large cells in vivo is a different and, at present, unresolved question. However, recent in vivo experimental evidence argues that this might be the case (Meaders *et al.*, 2020).

MATERIALS AND METHODS

Mold and device manufacturing

Multi-depth, three-dimensional (3D) printed microfluidic positive molds with deep fluid flow stabilization chambers (3648 × 1000 × 600 µm) and shallow fluid channels (2000 × 100 × 30 µm) were fabricated on preacrylated glass slides (microscope slides, 75 × 50 mm; Corning). The 3D printer (MAX X27; Asiga) used a 3D printing method for microfabrication, named stereolithography (SL), which is based on digital light processing (DLP; Lu *et al.*, 2006; Gross *et al.*, 2014; Gong *et al.*, 2015; Ho *et al.*, 2015). The process to manufacture a 3D multiheight mold is illustrated in Supplemental Figure S6A. First, a preacrylated glass slide was attached to the 3D printer build platform with double-sided tape. UV light was transmitted from the bottom of the resin tray to polymerize the first layer in accordance with the micromirror design (Supplemental Figure S6C). To make the next layer, the 3D printer adjusted its height and exposed the resin to UV light again, building upon the established layer. This continued until the desired mold, which is a positive relief of the microfluidic device, was finished being fabricated (Supplemental Figure S6D). The steps needed to turn the mold into a functional microfluidic device are shown in Supplemental Figure S6B. First, the mold was placed in a developing tank filled with isopropyl alcohol to flush away residual resins. This was followed by 5–10 min of UV curing, and then the mold was treated with oxygen plasma under 600 psi for 5 min to remove any remaining residual resin chemicals on the surface of the micropattern. Next, the mold and a weigh boat containing 50 µl fluorosilan were placed together in a desiccator for 3 h so that a thin layer of fluorosilan was uniformly deposited on the mold's surface. Once the surface treatment was completed, a PDMS elastomer (Dow Corning) containing a base and curing agent was poured into the mold and allowed to cure at room temperature for 2 d. Once cured, the PDMS replica was cut out and peeled off the resin mold (Supplemental Figure S6E). Holes were punched into the inlets and outlets with a sharpened 20G dispensing needle (Brico Medical Supplies). Finished microfluidic devices were made by bonding the PDMS replica to a coverslip (#1.5 thickness; Fisher Scientific) after oxygen plasma treatment (Duffy *et al.*, 1999; Supplemental Figure S6F).

Hydrogel polymers

The hydrogel annular cylinders, sawtooth arrays, 30° and 90°Vs, and teardrop structures were polymerized by using 30% (wt/wt) PEGDA in 1× CSF-XB (100 mM K[Cl], 0.1 mM $CaCl_2$, 1 mM $MgCl_2$, 50 mM sucrose, 10 mM HEPES, and 5 mM ethylene glycol tetraacetic acid (EGTA) at pH 7.7) with 1% (wt/wt) photoinitiator (lithium phenyl-2,4,6-trimethylbenzoylphosphinate, LAP). An IX81 Olympus microscope with attached micromirror array system (Polygon400 dense pixel; Mightex) was used in conjunction with an Olympus 20 × UPlanSApo (0.75 NA) air objective to expose hydrogel solutions to polymerizing UV light (405 nm) in microfluidic devices (Hahn *et al.*, 2006). PEGdiPDA (number average molecular weight ~4070 Da) was synthesized as described (Kloxin *et al.*, 2009; Kharkar *et al.*, 2015) and was mixed with 1× CSF-XB buffer at 10% (wt/wt) with 1% (wt/wt) LAP. This monomer was photopolymerized into a hydrogel polymer matrix by exposure to UV light (405 nm) with the micromirror system described above and was then photodegraded as needed by exposure to a lower wavelength (365 nm) (Fairbanks *et al.*, 2009).

Aster formation in *X. laevis* interphase extracts

X. laevis egg extracts were prepared from oocytes arrested in meiotic metaphase (Desai *et al.*, 1999; Maresca and Heald, 2006; Good and Heald, 2018). To induce interphase for aster formation and to block protein synthesis and prevent reentry into mitosis, 0.4 mM $CaCl_2$ and 100 µg/ml cycloheximide, respectively, were added to the arrested egg extract on ice. The extract was also supplemented with 150 nM mCherry-TMBD to label the MTs. The mCherry-TMBD fusion protein was produced and purified as described (Mooney *et al.*, 2017). Briefly, the plasmids were expressed in BL21 (DE3) cells, and the resulting fusion protein was purified on nickel spin columns (Bio-Rad). In experiments that inhibited functional dynein, 2 µM of p150-CC1 was added to the extract (Gaetz and Kapoor, 2004). For experiments in which MT growing ends were visualized, 60 nM EB1-GFP (Tirnauer *et al.*, 2002) was added to the interphase extract. To generate asters, aMTOCs (Tsai and Zheng, 2005), which consist of protein A Dynabeads (Invitrogen) coated in aurora A antibodies (a generous gift from T. Mitchison and C. Field, Harvard Medical School), were added to the egg extract. All experiments using egg extract were repeated at least three times using different extract preparations. All experiments involving *X. laevis* were conducted in accordance with the University of Wyoming and the Marine Biological Laboratory Institutional Animal Care and Use Committees' guidelines.

Microfluidic device preparation

To ensure that hydrogel structures adhered to the glass coverslips within our PDMS devices, a 2% (vol/vol) solution of 3-acryloxypropyltrimethoxysilane solution in 95% ethanol was flowed through each device for 5 min followed by a wash with 95% ethanol. Treated devices were subsequently baked at 75°C for 10 min and then washed again with 95% ethanol before being rinsed in ddH_2O and baked dry. After hydrogel structures had been made in the microfluidic devices, the glass on the interior of the microfluidic devices was passivated by incubation with 0.5% (wt/vol) pll(50)(HCl)-g(10)-mPEG(114) (pll-PEG; Nanosoft Polymers) in 1× CSF-XB buffer for at least 1 h at room temperature. For experiments using exposed aMTOCs, coverslips were passivated by exposing a device filled with poly(ethylene glycol)mono acrylate to UV light. This treatment results in a brush layer of PEG on the coverslip surface that hydrogel structures made from PEGDA and PEG-diPDA can adhere to. Afterward the remaining PEG-monoacrylate was washed out. Following this passivation, the devices were stored in 50-ml conical tubes containing 1× CSF-XB buffer overnight at room temperature to ensure that the device was well saturated to prevent fluid absorption and flow. Before the microfluidic device could be used, it had to be washed with ≥100 µl of 1× CSF-XB buffer. A 1-ml syringe (Norm-ject) connected to 0.10-in. tubing (Tygon) was filled with 1× CSF-XB buffer, and the tubing was inserted into the inlet to pump ≥100 channel volumes of buffer through the device. While the device was being washed, the egg extract was taken up into a fresh syringe and tubing. The tubing was inserted into the inlet of the microfluidic device, and the egg extract was pumped through at 5 µl/min using a syringe pump (Nemesys pumps; CETONI GmbH, Korbussen, Germany) in a 4°C room for 20 min. The device was brought to the cooled microscope room (16°C) on ice to ensure that MT polymerization did not occur prematurely. While still being kept cold, the glass coverslip was affixed to the cooling unit with VALAP (made by melting together equal weights of Vaseline, lanolin, and paraffin). The cooling unit consisted of a hollow, custom-fabricated metal rectangle through which ice water was continuously pumped. This maintained a steady temperature on the microscope stage over long time periods.

Imaging and analyses

Imaging was done on an Olympus IX81 confocal microscope equipped with a spinning-disk confocal head (CSU-X1; Yokogawa). Olympus 20 × UPlansSApo (0.85 NA) oil and 40 × UPlanFLn (1.3 NA) oil objectives were used to visualize MTs. An Olympus 60 × UPlanSApo (1.35 NA) oil objective was used to visualize EB1 comets interacting with the hydrogel barrier. For the channel experiments, 25-µm *z* stacks (taken at 5 µm intervals) were generated for each of the positions every 5 min and the plane with a visible aMTOC was used. For experiments using hydrogel lobster traps and V-shaped barriers, single-plane images were taken every minute and asters were tracked only after their MTs made contact with the nearest wall. The same was done for the annular cylinders, but images were taken every 30 s. Images were processed and analyzed using Fiji (National Institutes of Health; http://rsb.info.nih.gov/ij/) to manually get the coordinates of the aMTOC to track aster movement. Images were background subtracted based on the signal seen in the hydrogel structures alone and cropped. The enhanced contrast feature in Fiji (saturated pixel 0.4%) was used on the time-lapse videos to consistently adjust the LUT for aster images in all of the montages. Aster motion was calculated based on the aMTOC coordinates measured in Fiji, which were imported into GraphPad Prism (version 8; GraphPad Software) to make both the series of line traces and the line graphs with 95% confidence intervals. The CoMM was calculated using Fiji. First the images were background subtracted to remove signal from extract devoid of MTs. Images were then smoothed using a rolling ball filter (radius = 5 pixels) and segmented based on the MT signal such that the segmentation resulted in a single, contiguous region of interest (ROI) for MTs associated with the aster. The Center of Mass function of the measure tool in Fiji was then applied and produced the coordinates of the ROI's center of mass. Then the aMTOC coordinates were subtracted from the CoMM to find the difference. The velocities to be graphed relative to this difference and to the proximity to the nearest barrier were found by taking the slope at 5-min intervals from the 30°V and 90°V plots in Figure 3D.

ACKNOWLEDGMENTS

We thank Tim Mitchison and Christine Field for their generous gift of the Aurora A antibody used in these studies. We also thank Priscilla Phan for preparation of *Xenopus* extracts and Mirek Tomschik for expressing and purifying many of the recombinant proteins used. A special thanks goes to David Burgess and Johnathan Meaders, who offered numerous insights and provided many enlightening discussions about the physics of aster centration. We also express our gratitude to Amy Fluet for her thoughtful editing and comments on manuscript drafts. Special thanks goes out to Daniel Zhu for his efforts to help with data alignment and processing methods and to Marko Horb and the Xenopus National Resource at the Marine Biological Laboratory. This work was made possible by an Institutional Development Award (IDeA) from the National Institute of General Medical Sciences (NIGMS) of the National Institutes of Health (grant #2P20GM103432). It was also supported by additional funding provided by the NIGMS (grant #R01GM113028), the Biomedical Scholars program of the Pew Charitable Trusts, and the Marine Biological Laboratory Whitman Center.

REFERENCES

Adames NR, Cooper JA (2000). Microtubule interactions with the cell cortex causing nuclear movements in Saccharomyces cerevisiae. J Cell Biol 149, 863–874.

Aist JR, Liang H, Berns MW (1993). Astral and spindle forces in PtK2 cells during anaphase B: a laser microbeam study. J Cell Sci 104 (Pt 4), 1207–1216.

Bisht J, LeValley P, Noren B, McBride R, Kharkar P, Kloxin A, Gatlin J, Oakey J (2019). Light-inducible activation of cell cycle progression in Xenopus egg extracts under microfluidic confinement. Lab Chip 19, 3499–3511.

Brangwynne CP, MacKintosh FC, Kumar S, Geisse NA, Talbot J, Mahadevan L, Parker KK, Ingber DE, Weitz DA (2006). Microtubules can bear enhanced compressive loads in living cells because of lateral reinforcement. J Cell Biol 173, 733–741.

Brito DA, Strauss J, Magidson V, Tikhonenko I, Khodjakov A, Koonce MP (2005). Pushing forces drive the comet-like motility of microtubule arrays in Dictyostelium. Mol Biol Cell 16, 3334–3340.

Chang F, Atilgan E, Burgess D, Minc N (2014). Manipulating cell shape by placing cells into micro-fabricated chambers. Methods Mol Biol 1136, 281–290.

Cheng X, Ferrell JE Jr (2019). Spontaneous emergence of cell-like organization in Xenopus egg extracts. Science 366, 631–637.

Decker F, Oriola D, Dalton B, Brugues J (2018). Autocatalytic microtubule nucleation determines the size and mass of Xenopus laevis egg extract spindles. eLife 7, e31149.

Desai A, Murray AW, Mitchison T, Walczak CE (1999). The use of Xenopus egg extracts to study mitotic spindle assembly and function. Methods Cell Biol 61, 385–412.

Dogterom M, Kerssemakers JW, Romet-Lemonne G, Janson ME (2005). Force generation by dynamic microtubules. Curr Opin Cell Biol 17, 67–74.

Dogterom M, Yurke B (1997). Measurement of the force-velocity relation for growing microtubules. Science 278, 856–860.

Duffy DC, Schueller OJA, Brittain ST, Whitesides GM (1999). Rapid prototyping of microfluidic switches in poly(dimethyl siloxane) and their actuation by electro-osmotic flow. J Micromech Microeng 9, 211–217.

Fairbanks BD, Schwartz MP, Bowman CN, Anseth KS (2009). Photoinitiated polymerization of PEG-diacrylate with lithium phenyl-2,4,6-trimethylbenzoylphosphinate: polymerization rate and cytocompatibility. Biomaterials 30, 6702–6707.
Field CM, Nguyen PA, Keisuke I, Groen AC, Mitchison TJ (2014). Xenopus cytoplasm with intact actin. Methods Enzymol 540, 399–415.
Field CM, Pelletier JF, Mitchison TJ (2019). Disassembly of actin and keratin networks by Aurora B kinase at the midplane of cleaving Xenopus laevis eggs. Curr Biol 29, 1999–2008.e1994.
Gaetz J, Kapoor TM (2004). Dynein/dynactin regulate metaphase spindle length by targeting depolymerizing activities to spindle poles. J Cell Biol 166, 465–471.
Gatlin JC, Matov A, Groen AC, Needleman DJ, Maresca TJ, Danuser G, Mitchison TJ, Salmon ED (2009). Spindle fusion requires dynein-mediated sliding of oppositely oriented microtubules. Curr Biol 19, 287–296.
Geisterfer ZM, Zhu DY, Mitchison TJ, Oakey J, Gatlin JC (2020). Microtubule growth rates are sensitive to global and local changes in microtubule plus-end density. Curr Biol 30, 3016–3023.
Gonczy P, Pichler S, Kirkham M, Hyman AA (1999). Cytoplasmic dynein is required for distinct aspects of MTOC positioning, including centrosome separation, in the one cell stage Caenorhabditis elegans embryo. J Cell Biol 147, 135–150.
Gong H, Beauchamp M, Perry S, Woolley AT, Nordin GP (2015). Optical approach to resin formulation for 3D printed microfluidics. RSC Adv 5, 106621–106632.
Good MC, Heald R (2018). Preparation of cellular extracts from Xenopus eggs and embryos. Cold Spring Harb Protoc 2018, pdb.prot097055.
Gross BC, Erkal JL, Lockwood SY, Chen C, Spence DM (2014). Evaluation of 3D printing and its potential impact on biotechnology and the chemical sciences. Anal Chem 86, 3240–3253.
Hahn MS, Taite LJ, Moon JJ, Rowland MC, Ruffino KA, West JL (2006). Photolithographic patterning of polyethylene glycol hydrogels. Biomaterials 27, 2519–2524.
Hara Y, Merten CA (2015). Dynein-based accumulation of membranes regulates nuclear expansion in Xenopus laevis egg extracts. Dev Cell 33, 562–575.
Ho CM, Ng SH, Li KH, Yoon YJ (2015). 3D printed microfluidics for biological applications. Lab Chip 15, 3627–3637.
Holy TE, Dogterom M, Yurke B, Leibler S (1997). Assembly and positioning of microtubule asters in microfabricated chambers. Proc Natl Acad Sci USA 94, 6228–6231.
Hyman AA (1989). Centrosome movement in the early divisions of Caenorhabditis elegans: a cortical site determining centrosome position. J Cell Biol 109, 1185–1193.
Ishihara K, Korolev KS, Mitchison TJ (2016). Physical basis of large microtubule aster growth. eLife 5, e19145.
Ishihara K, Nguyen PA, Groen AC, Field CM, Mitchison TJ (2014). Microtubule nucleation remote from centrosomes may explain how asters span large cells. Proc Natl Acad Sci USA 111, 17715–17722.
Juniper MPN, Weiss M, Platzman I, Spatz JP, Surrey T (2018). Spherical network contraction forms microtubule asters in confinement. Soft Matter 14, 901–909.
Kharkar PM, Kiick KL, Kloxin AM (2015). Design of thiol- and light-sensitive degradable hydrogels using Michael-type addition reactions. Polym Chem 6, 5565–5574.
Kimura A, Onami S (2005). Computer simulations and image processing reveal length-dependent pulling force as the primary mechanism for C. elegans male pronuclear migration. Dev Cell 8, 765–775.
Kimura K, Kimura A (2011). Intracellular organelles mediate cytoplasmic pulling force for centrosome centration in the Caenorhabditis elegans early embryo. Proc Natl Acad Sci USA 108, 137–142.
Kloxin AM, Kasko AM, Salinas CN, Anseth KS (2009). Photodegradable hydrogels for dynamic tuning of physical and chemical properties. Science 324, 59–63.
Kotak S, Busso C, Gonczy P (2012). Cortical dynein is critical for proper spindle positioning in human cells. J Cell Biol 199, 97–110.
Kotak S, Gonczy P (2013). Mechanisms of spindle positioning: cortical force generators in the limelight. Curr Opin Cell Biol 25, 741–748.
Laan L, Husson J, Munteanu EL, Kerssemakers JW, Dogterom M (2008). Force-generation and dynamic instability of microtubule bundles. Proc Natl Acad Sci USA 105, 8920–8925.
Laan L, Pavin N, Husson J, Romet-Lemonne G, van Duijn M, Lopez MP, Vale RD, Julicher F, Reck-Peterson SL, Dogterom M (2012a). Cortical dynein controls microtubule dynamics to generate pulling forces that position microtubule asters. Cell 148, 502–514.
Laan L, Roth S, Dogterom M (2012b). End-on microtubule-dynein interactions and pulling-based positioning of microtubule organizing centers. Cell Cycle 11, 3750–3757.
Labbe JC, McCarthy EK, Goldstein B (2004). The forces that position a mitotic spindle asymmetrically are tethered until after the time of spindle assembly. J Cell Biol 167, 245–256.
Lammers LG, Markus SM (2015). The dynein cortical anchor Num1 activates dynein motility by relieving Pac1/LIS1-mediated inhibition. J Cell Biol 211, 309–322.
Letort G, Nedelec F, Blanchoin L, Thery M (2016). Centrosome centering and decentering by microtubule network rearrangement. Mol Biol Cell 27, 2833–2843.
LeValley PJ, Noren B, Kharkar PM, Kloxin AM, Gatlin JC, Oakey J (2018). Fabrication of functional biomaterial microstructures by in situ photopolymerization and photodegradation. ACS Biomater Sci Eng 4, 3078–3087.
Lu Y, Mapili G, Suhali G, Chen S, Roy K (2006). A digital micro-mirror device-based system for the microfabrication of complex, spatially patterned tissue engineering scaffolds. J Biomed Mater Res A 77, 396–405.
Maresca TJ, Heald R (2006). Methods for studying spindle assembly and chromosome condensation in Xenopus egg extracts. Methods Mol Biol 322, 459–474.
McNally FJ (2013). Mechanisms of spindle positioning. J Cell Biol 200, 131–140.
Meaders JL, Burgess DR (2020). Microtubule-based mechanisms of pronuclear positioning. Cells 9, 505.
Meaders JL, Norton de Matos S, Burgess DR (2020). A pushing mechanism for microtubule aster positioning in a large cell type. Cell Rep, https://doi.org/10.1016/j.celrep.2020.108213.
Minc N, Burgess D, Chang F (2011). Influence of cell geometry on division-plane positioning. Cell 144, 414–426.
Mitchison TJ, Maddox P, Gaetz J, Groen A, Shirasu M, Desai A, Salmon ED, Kapoor TM (2005). Roles of polymerization dynamics, opposed motors, and a tensile element in governing the length of Xenopus extract meiotic spindles. Mol Biol Cell 16, 3064–3076.
Mooney P, Sulerud T, Pelletier JF, Dilsaver MR, Tomschik M, Geisler C, Gatlin JC (2017). Tau-based fluorescent protein fusions to visualize microtubules. Cytoskeleton (Hoboken) 74, 221–232.
Nazockdast E, Rahimian A, Needleman D, Shelley M (2017). Cytoplasmic flows as signatures for the mechanics of mitotic positioning. Mol Biol Cell 28, 3261–3270.
Nguyen-Ngoc T, Afshar K, Gonczy P (2007). Coupling of cortical dynein and G alpha proteins mediates spindle positioning in Caenorhabditis elegans. Nat Cell Biol 9, 1294–1302.
Nuttelman CR, Mortisen DJ, Henry SM, Anseth KS (2001). Attachment of fibronectin to poly(vinyl alcohol) hydrogels promotes NIH3T3 cell adhesion, proliferation, and migration. J Biomed Mater Res 57, 217–223.
Okumura M, Natsume T, Kanemaki MT, Kiyomitsu T (2018). Dynein-dynactin-NuMA clusters generate cortical spindle-pulling forces as a multi-arm ensemble. eLife 7, e36559.
Park DH, Rose LS (2008). Dynamic localization of LIN-5 and GPR-1/2 to cortical force generation domains during spindle positioning. Dev Biol 315, 42–54.
Pelletier J, Field C, Furthauer S, Sonnett M, Mitchison T (2020). Co-movement of astral microtubules, organelles and F-actin suggests aster positioning by surface forces in frog eggs. bioRxiv. doi: 10.1101/2020.06.17.154260.
Petry S, Groen AC, Ishihara K, Mitchison TJ, Vale RD (2013). Branching microtubule nucleation in Xenopus egg extracts mediated by augmin and TPX2. Cell 152, 768–777.
Rappaport R, Rappaport BN (1994). Cleavage in conical sand dollar eggs. Dev Biol 164, 258–266.
Reinsch S, Gonczy P (1998). Mechanisms of nuclear positioning. J Cell Sci 111 (Pt 16), 2283–2295.
Roth S, Laan L, Dogterom M (2014). Reconstitution of cortical dynein function. Methods Enzymol 540, 205–230.
Tanimoto H, Kimura A, Minc N (2016). Shape-motion relationships of centering microtubule asters. J Cell Biol 212, 777–787.
Tanimoto H, Salle J, Dodin L, Minc N (2018). Physical forces determining the persistency and centering precision of microtubule asters. Nat Phys 14, 848–854.
Tirnauer JS, Grego S, Salmon ED, Mitchison TJ (2002). EB1-microtubule interactions in Xenopus egg extracts: role of EB1 in microtubule stabilization and mechanisms of targeting to microtubules. Mol Biol Cell 13, 3614–3626.

Tran PT, Marsh L, Doye V, Inoue S, Chang F (2001). A mechanism for nuclear positioning in fission yeast based on microtubule pushing. J Cell Biol 153, 397–411.

Tsai MY, Zheng Y (2005). Aurora A kinase-coated beads function as microtubule-organizing centers and enhance RanGTP-induced spindle assembly. Curr Biol 15, 2156–2163.

Wu HY, Nazockdast E, Shelley MJ, Needleman DJ (2017). Forces positioning the mitotic spindle: theories, and now experiments. Bioessays 39, bies.201600212.

Wuhr M, Dumont S, Groen AC, Needleman DJ, Mitchison TJ (2009). How does a millimeter-sized cell find its center? Cell Cycle 8, 1115–1121.

Wuhr M, Tan ES, Parker SK, Detrich HW 3rd, Mitchison TJ (2010). A model for cleavage plane determination in early amphibian and fish embryos. Curr Biol 20, 2040–2045.

Zhu J, Burakov A, Rodionov V, Mogilner A (2010). Finding the cell center by a balance of dynein and myosin pulling and microtubule pushing: a computational study. Mol Biol Cell 21, 4418–4427.